Journal of Solid State Chemistry **156,** 88–100 (2001)
doi:10.1006/jssc.2000.8967, available online at http://www.idealibrary.com on IDEAL®

Computer Modeling and Description of Nonstoichiometric Apatites $Cd_{5-\eta/2}(VO_4)_3I_{1-\eta}$ and $Cd_{5-\eta/2}(PO_4)_3Br_{1-\eta}$ as Modified Chimney–Ladder Structures with Ladder–Ladder and Chimney–Ladder Coupling

Andrew G. Christy,*,[1,2] Peter Alberius-Henning,†,[3] and Sven A. Lidin†

*Research School of Chemistry, Australian National University, Canberra ACT 0200, Australia; and †Arrhenius Laboratory, Department of Inorganic Chemistry, Stockholm University, S-106 91 Stockholm, Sweden

Received May 8, 2000; in revised form August 18, 2000; accepted September 15, 2000; published online December 21, 2000

Diffraction patterns from apatite-structure compounds $Cd_{5-\eta/2}(TO_4)_3X_{1-\eta}$ with T = P, V and X = Br, I show sheets of diffuse scattering normal to c* at incommensurate $l = q$ ($q = 1.63$ for Cd–V–I apatite and $q = 1.78$ for Cd–P–Br apatite), because the c repeat of the average unit cell is shorter than two X diameters. The equilibrium $X..X$ spacing along c defines the incommensurate periodicity c/q and stoichiometry $(1-\eta) = q/2$. The layers show a honeycomb texture for the Cd–V–I apatite, which is condensed into discrete spots for the Cd–P–Br compound. In both phases, $X..X$ repulsions along $\langle 100 \rangle$ force neighboring rods of X atoms out of phase. In the Cd–P–Br phase, additional $\langle 210 \rangle$ attractions drive incipient formation of a rhombohedral superstructure. Average structure site occupancies and the observation of second-order diffuse layers at both $l = 2q$ and $l = q+2$ imply the existence of strong Cd..X in addition to $X..X$ interactions. A three-dimensional computer model was used to produce finite-temperature structure simulations as a function of $X..X$ interactions along $\langle 001 \rangle$, $\langle 100 \rangle$, and $\langle 210 \rangle$, and X..Cd interactions, from which diffraction patterns were calculated. The experimental patterns were fit and approximate values for the interaction energies obtained (hundreds to thousands of joules per mole). It was apparent that lock-in to commensurability caused by the X..Cd term and the formation of nonprimitive incommensurate modulated structures driven by $X..X$ interactions were mutually antagonistic, and the actual structures are compromises between the two. © 2001 Academic Press

Key Words: **apatite; nonstoichiometric compounds; short-range order; diffuse scattering; incommensurate structure; modulated structure; computer simulation.**

INTRODUCTION

The apatite group of minerals includes about 30 naturally occurring species that are structurally isotypic with fluorapatite, $Ca_5(PO_4)_3F$. The type compound is the largest single source on the planet of phosphate for industrial use. Its hydroxyl analogue is a major constituent of hard biological materials such as bone and tooth enamel. Pb analogues are minor commercial sources of lead, and are also of interest as potential stable repositories for heavy metals in the environment.

The apatite structure $(A1)_2^{[9]}(A2)_3^{[6+1]}(TO_4)_3X$ is formed by a wide range of synthetic compounds with one or two moderately large A cations (Na^+, K^+, Ca^{2+}, Sr^{2+}, Ba^{2+}, Y^{3+}, REE^{3+}, Th^{4+}, Mn^{2+}, Cd^{2+}, Tl^+, Pb^{2+}, Bi^{3+}), tetrahedral T cations (Si^{4+}, Ge^{4+}, P^{5+}, V^{5+}, As^{5+}, S^{6+}, Cr^{6+}), and anionic X (F^-, Cl^-, Br^-, I^-, OH^-, O^{2-}, S^{2-}, Se^{2-}, N^{3-}, CuO^-, $\square$ = vacancy). The TO_4^{n-} unit has also been replaced by BeF_4^{2-} and ReO_5^{3-}. It may also be replaced by CO_3^{2-} in some natural apatites although the precise structural role of the carbonate remains controversial. A comprehensive list of apatites in the literature, with references, is provided in Alberius-Henning (1).

The ideal apatite structure (2) has a hexagonal unit cell with space group $P6_3/m$, $Z = 2$, $a = 10.0 \pm 0.7$ Å, and $c = 7.0 \pm 0.5$ Å. The $(A2)_3(TO_4)_3$ part of the structure forms dense ribbons running parallel to **c**, in which the oxygens approximate close-packing. Between the ribbons there are two types of channels at $[0\,0\,z]$ and $\pm[\frac{2}{3}\,\frac{1}{3}\,z]$. The X anions are situated in the former channels, and the large $A1$ cations in the latter (Fig. 1).

There is considerable scope for structural variation in the apatite structure. Extensive solid solution is known to occur on the A sites (e.g., Ca↔Pb), the T sites (e.g., SiS↔PP), and the X sites. Partial occupancy also occurs in some compounds. These substitutions can give rise to ordering and superstructure formation. Displacive distortion of the structure also occurs. Many apatites are known in which the

[1] To whom correspondence should be addressed. Fax: + 61 2 6249 0750. E-mail: christy@rsc.anu.edu.au.

[2] Current address: Department of Applied Mathematics, Research School of Physical Science and Engineering, Australian National University, Canberra ACT 0200, Australia.

[3] Current address: Department of Chemistry, University of California at Santa Barbara, Santa Barbara, CA 93106.

0022-4596/01 $35.00

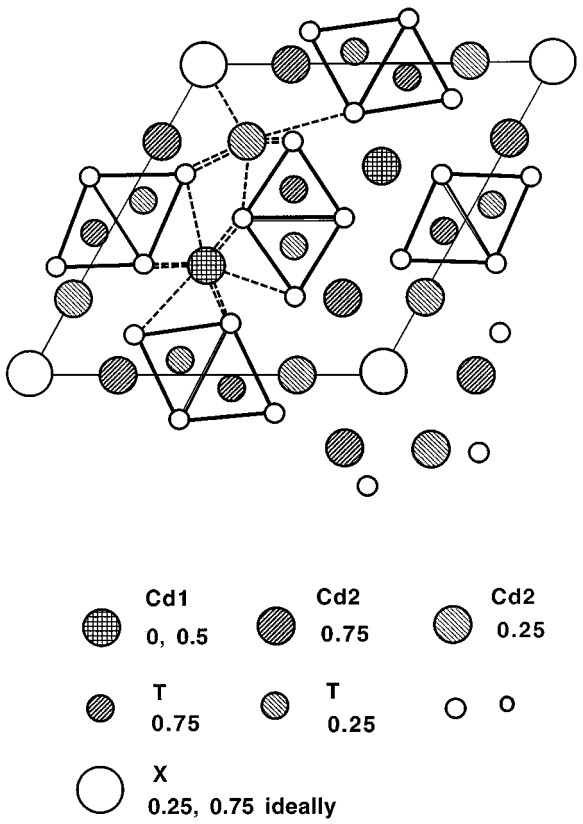

FIG. 1. Ideal apatite structure projected down **c**. Fractional z coordinates for atoms are indicated in the key.

large size (Cl^-, S^{2-}) or dipolar nature (OH^-) of the X groups causes displacement of the X along **c**, with concomitant loss of translational and/or rotational symmetry. Previously known and new examples of such apatites are discussed in detail by Alberius-Henning (1).

Apatite structure compounds $A_5(TO_4)_3X$ with small A cations and large X anions necessarily have relatively small $c/2$ distances between the ideal $z = \pm 0.25$ positions of the X atoms. In the case of Cd apatites with $X =$ Br or I, this distance is considerably less than the sum of two anionic radii for these elements (3). This is apparent even when the relatively small "crystal radii" of Shannon (4) are used (Table 1). The X atoms are therefore displaced away from the ideal positions, and some X vacancies are required as shown in Fig. 2. Electric charge is presumably balanced by Cd deficiency leading to the stoichiometry $Cd_{5-\eta/2}(TO_4)_3X_{1-\eta}$. Three-dimensional average structures were refined by Sudarsanan *et al.* (3) for the compounds with $T =$ V and $X =$ I, and $T =$ P, As, V with $X =$ Br. The extensively displaced X atoms were distributed over sextuply split sites in a complex fashion, discussed in more detail in (5). Slightly reduced occupancy was calculated for the Cd sites, but the total Cd vacancy did not in general balance the charge deficit on the X sites exactly, and no systematic partioning

TABLE 1
$X..X$ spacings and X Partial Occupancy $(1-\eta)$ in Cd–P–Br and Cd–V–I apatite

	Cd–P–Br	Cd–V–I
c/Å[a]	6.468	6.496
q	1.78	1.63
c/q	3.634	3.985
$2r_{X^-}$/Å[b]	3.64	4.12
$c/2r_{X^-}$	1.78	1.58
$(1-\eta)_{max}$	0.890	0.815
$(1-\eta)^a_{obs}$	0.830(19)	0.734(9)

[a] Sudarsanan *et al.* (3).
[b] Shannon (4).

of vacancies was observed between the Cd1 sites (4*f*, $[\frac{2}{3}, \frac{1}{3}, z \approx 0]$) and the Cd2 sites (6*h*, $[x \approx \frac{1}{4}, y \approx 0, \frac{1}{4}]$).

Extensive, structured diffuse X-ray scattering has been found in the diffraction patterns of Cd–P–Br apatite and Cd–V–I apatite (1). The additional spots in the pattern of the Cd–P–Br phase were refined as Bragg peaks, and the structure was described as a four-dimensional incommensurate modulated structure (6). The observed scattering was primarily due to displacements of the strongest scatterers, the Br^- anions, away from the ideal positions of the fluorapatite structure. However, the additional diffraction spots are diffuse, so the modulated structure of (6) represents a greater degree of long-range order than is present in the real structure. In this paper, we use a computer simulation of the anion arrangement to calculate diffuse scattering patterns and model the short-range ordering behavior in real space. This approach allows us also to characterize the ordering that causes the diffuse scattering of the Cd–V–I apatite, which is not concentrated into spots, and is not amenable to conventional structure refinement. We show that both types of scattering can be caused by the same small set of interatomic interactions, with different relative signs and strengths, and also examine the range of scattering behaviors that can be produced by these interactions, and which may be encountered in other apatite phases.

The incommensurate spacing of the halide anions in (6) suggests a structure of "chimney–ladder" type in which "ladders" (rods of Br^- in this case) have a periodicity different from that of the host "chimneys." The term "chimney–ladder" for such structures originated with Pearson (7), who used it to describe similarly incommensurate or Vernier-commensurate intermetallics such as those of Nowotny and co-workers (8, 9). Other examples of similar behavior include a recently described high-pressure polymorph of Ba (10), $NbTe_4$ (11), and the two-dimensional discommensuration in $Hg_{3-\eta}AsF_6$ (12). Chimney–ladder interactions may be ionically bonding as in the apatites of this study, metallic

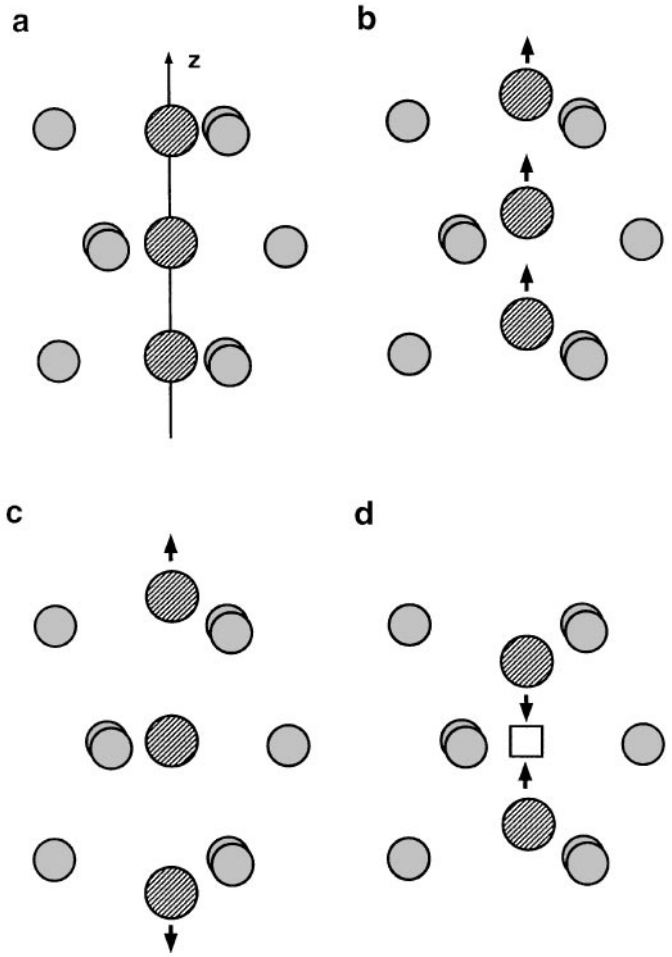

FIG. 2. Styles of X displacement along **c** in apatites. (a) "Ideal" fluorapatite. X atom is at $z = 0.25$, coplanar with triangles of Cd2. (b) Cl and OH apatites. X is displaced toward the octahedral site. X displacements are often modulated along the **a** direction in such systems. (c) and (d) Br and I apatites of this study. $X..X$ is larger than $c/2$. Some X vacancies are required.

as in the other examples cited above, or pure van der Waals in molecular host–guest inclusion structures such as the alkane-included urea compounds of Welberry and Mayo (13).

EXPERIMENTAL

The possibility of short-range ordering of X atom displacements and occupancies renders the Cd apatites prime candidates for diffuse scattering behavior. This was confirmed by electron diffraction (1). Single crystals suitable for X-ray study were then grown in Pt crucibles contained in evacuated quartz tubes, in an excess of molten $CdBr_2$ and CdI_2 as appropriate. The Cd–P–Br apatite was grown at 1023 K over 4 days, the Cd–V–I compound at 1013 K over 2 days. The solid reactants added to the flux were $Cd_3(PO_4)_2$ and $CdO + V_2O_5$, respectively. Excess flux and other products were separated from the apatite crystals by water dissolution. The residual apatite crystals were hexagonal prisms approximately 0.3 mm × 0.05 mm in size (1, 6). X-ray data sets collected at 150 K on a STOE image plate detector system using a Mo sealed tube source (1, 6). Diffuse planes normal to **c*** were observed for both compounds of this study. These were incommensurate with the c^* reciprocal lattice repeat of the host Cd–T–O framework. The V–I compound shows layers of diffuse scattering at $\pm qc^*$ where $q = 1.63$ (Fig. 3a). In the case of the P–Br compound, the first-order diffuse planes lie at $q = 1.78$ (Fig. 3b). The values of q are well estimated by the ratio $c/2r_{X^-}$, where r_{X^-} is the Shannon crystal radius for the halide (Table 1). The intensity in the incommensurate planes of the V–I apatite forms a continuous "honeycomb" network (Fig. 3c), whereas that in the P–Br compound is condensed into discrete broad spots centered on $(\frac{1}{3}\ \frac{1}{3}\ q)$ and related positions in reciprocal space (Fig. 3d), connected by faint honeycomb streaks.

From inspection of the experimental diffuse scattering, it was possible to deduce aspects of the real-space structure that were most important in producing the observed diffuse phenomena. Preliminary deductions from the experimental diffraction patterns were as follows.

(i) The strongest scattering occurs in layers normal to **c*** at $l = \pm q$, implying that strongly scattering species form rods along **c** and are separated by a well-defined average vector $[0,\ 0,\ c/q]$. Since the average structure indicates a broad spread of the z coordinate for only the X anions (3, 5, 6), $\mathbf{c}/q$ was taken to be the mean vector between X along a $[0\ 0\ z]$ rod.

(ii) There was no diffuse scattering in the $l = 0$ layer. This implies that the local structure is identical with the average structure when projected down [001]. Hence, the X contents of all $[0\ 0\ z]$ rods are the same, and the only significant correlated displacements are along the **c** direction.

(iii) The honeycomb texture and condensation into spots exhibited by the experimental diffuse scattering layers indicate that phase correlations exist between rods, which arise from effective $X..X$ interactions in the xy plane.

(iv) If the z coordinates of the X array were fully incommensurate with the Cd–T–O host "chimney," then the average structure would show uniform delocalization of X along the **c** direction. This is not observed in the refinements of (3, 5, 6), which all indicate a preference for the X anions to lie near the Cd2 triangles at $z = 0.25$. Clearly, Cd..X interactions perturb the X z coordinates. Further evidence for this is provided by the occurrence of second-order diffuse layers at $l = q + 2$ in addition to $l = 2q$ in our experimental patterns. In fact, for Cd–P–Br apatite, the $l = q + 2$ layer is the more intense.

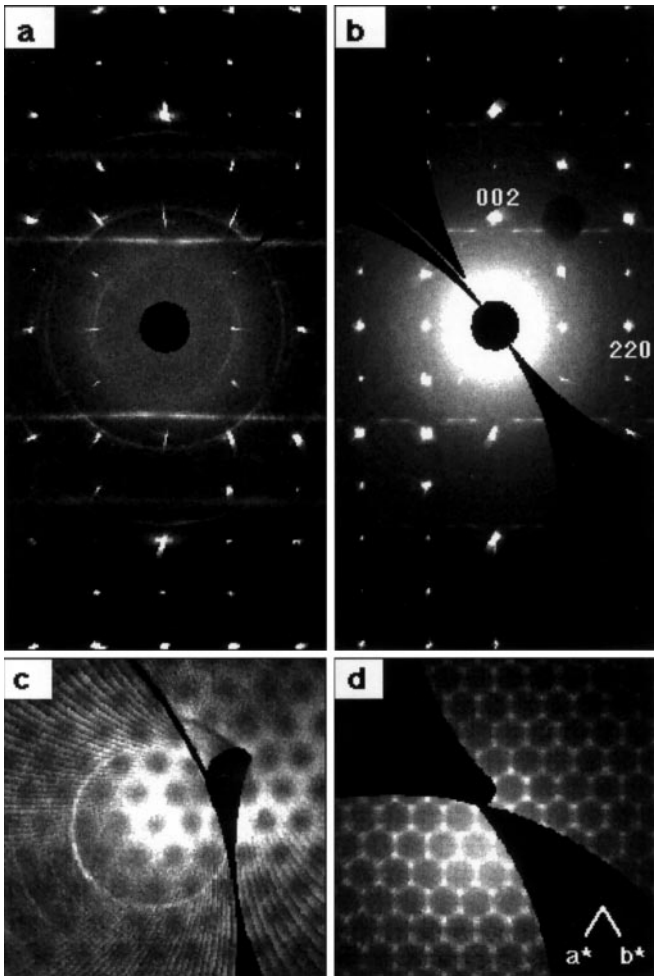

FIG. 3. Experimental X-ray diffraction patterns: (a) *hhl* section for V–I apatite (b) *hhl* section of reciprocal space for P–Br apatite; (c) *hk* 1.63 layer for V–I apatite; and (d) *hk* 1.78 layer for P–Br apatite.

Computer Simulation

The aim of the computer simulation was to produce the simplest possible model structure capable of reproducing the salient features of the observed diffuse scattering patterns, using the minimum number of distinct types of scattering species and interactions between them, rather than to model the structure and its energetics comprehensively. The short-range ordered structures produced by the model have an associated energy which in general is a function of occupational and displacive two-body correlations (which relate directly to diffraction features). The correlations in turn can be regarded as consequences of *effective* two-body potentials although it should be noted that such potentials are resultant of a large number of specific interatomic interactions involving the two bodies and their neighbors, including atoms that are not explicitly depicted in the model. Each simulation used preset magnitudes for a minimum of such potentials and then displaced X anions until the structure was equilibrated. The diffraction pattern was then calculated.

It was necessary for the model to incorporate at least the interactions implied by deductions (i)–(iv) proposed above. Deductions (i) and (ii) imply that the X anions should have a well-defined mean periodicity along any single $[0\ 0\ z]$ rod, but with period c/q incommensurate with that of the host Cd–T–O framework. Since the periodicity is not perfect, a displacement from the ideal incommensurate position is associated with each X.

If the relative phases of the different "ladder" rods were uncorrelated, the scattering within any given diffuse layer in reciprocal space would vary slowly and monotonically with diffraction angle and would not show periodic modulation such as the observed honeycomb texture. The simplest possible phase correlation between rods would be produced by attractive forces along $\langle 100 \rangle$ directions, giving a primitive hexagonal array of X atoms. Because of the triangular connectivity of the rod packing, *repulsive* $\langle 100 \rangle$ forces would be mutually frustrating, and fail to produce ordered superstructures. However, longer-range (e.g., second-nearest-neighbor) interactions can stabilize three-dimensionally periodic X arrangements in the presence of repulsive $\langle 100 \rangle$ interactions. In the extreme ordered case, the diffraction patterns from such structures would include sharp modulation peaks from the X substructure, and the full structure would be defined by a four-dimensional modulated description. The refinement of the Cd–P–Br apatite (1, 6) approximates the real structure in this way. In the absence of Cd..X interactions, the displacements δz of successive X anions away from the average position of the ideal fluorapatite structure ($z = n \pm 0.25$, integral n) would form a sawtooth waveform, increasing linearly with ideal position until $\delta z > 0.25$, at which point the mapping of actual X anions onto ideal fluorapatite sites would have a discontinuity, leaving a vacancy. The refinement of (1, 6) for the Cd–P–Br phase additionally truncated the permissible values of z so as to avoid z values near 0 and 0.5. This approximated the effect of strong Cd..X interactions perturbing the X substructure. However, such a modulation would imply a Cd..X interaction that was a flat boxlike potential with infinitely high walls around the forbidden range of z values, which is unphysical. Simulations using a box potential were found to give unrealistically intense high-order layers, and we believe that the model presented in this paper gives a more accurate portrayal of the true short-range structure and associated diffuse scattering. Specific details of the model are as follows.

A $60 \times 60 \times 100$ array $\{u, v, w\}$ of X anion sites was constructed with primitive hexagonal geometry and cyclic boundary conditions. Each X site had an associated w displacement parameter. Initially, all displacements δw within a given $[u, v]$ rod were set to the same uniform variate ranging from -0.5 to $+0.5$, but the values for different

$[u, v]$ were uncorrelated. The values of δw for individual X sites were then relaxed using a Monte Carlo algorithm. In each step of the relaxation routine, a $[u, v, w]$ site was randomly selected and its energy calculated. The change in energy ΔE on making a small random change to δw was calculated, and then accepted with probability $p = 1$ for $\Delta E < 0$ and $p = e^{-\Delta E}$ for $\Delta E > 0$. "Simulated annealing," in which a progressive reduction in energy scale factor occurs, was *not* employed in order to simulate the effect of thermal disorder at constant temperature. Terms contributing to the site energy were as follows.

(i) An $X..X$ interaction along [001]. This represents the nonbonded interaction between X's that are linked via Cd neighbors. Characteristics of an appropriate potential should include strong repulsion between X's at distances less than equilibrium, but a weak attraction at long range. A Lennard-Jones potential E_z between neighboring X's at $[u, v, w]$ and $[u, v, w \pm 1]$ was used. This took the form $E = E_z(-2/d^6 + 1/d^{12})$, giving an equilibrium interionic distance of 1 unit (the repeat of the average X substructure) and potential depth E_z.

(ii) $X..X$ potentials E_x to the six nearest neighbors along approximate $\langle 100 \rangle$ directions and E_y to six second-nearest neighbors along $\langle 210 \rangle$ directions. The $X..X$ distances of 10–18 Å render direct interactions negligible. However, both structure determination (14) and calculations (15) indicate that X displacements in apatites couple strongly to relaxations of the cations and oxide anions. Such relaxations of these other species can mediate $X..X$ coupling even if they do not themselves contribute strongly to the X-ray scattering. The form of potential selected was a Gaussian function, $E = E_x \exp(-10\delta t^2)$, where $\delta t = (w + \delta w) - (w' + \delta w')$. Without explicity forcing a w periodicity on the potential, this was found to approximate the shape of a cosine potential over the δt range $-0.5 < \delta t < +0.5$ quite well.

(iii) A Cd..X potential, E_{Cd}. The height $t = w + \delta w$ of the central atom was rescaled into a z coordinate on the axial system of the apatite host substructure: $z = (t - 5)/q$ where the "5" is an offset between origins introduced to avoid edge effects if cyclic boundary conditions on the $\{u, v, w\}$ array were relaxed. Since the Cd2 triangles repeat periodically along the **c** direction, a sinusoidal potential was chosen. The energy term was of the form $E = -E_{Cd} \cos 4\pi z$, with maxima at the Cd2 z coordinates $z = n \pm 0.25$ (n integral).

After $60 \times 60 \times 100$ "steps," a "cycle" was completed, in which each $[u, v, w]$ site had been examined once on average. After 50 such cycles, output statistics were stable or oscillated with small amplitudes, indicating that satisfactory equilibration had been achieved. In order to produce an output file of structure data, the X anion substructure was transplanted onto a simulated apatite host structure. This was a $40 \times 40 \times 40$ array of simulated apatite unit cells $\{x, y, z\}$. A fourth index s indicated site number. Each set of indices $\{x, y, z, s\}$ addressed an "occupation array" containing binary occupation data for each site, and a displacement array containing displacements of atoms away from the ideal z coordinate of the site. It was found that in order to calculate the X anion contribution to the average scattering correctly, the X had to be distributed over a large number of split-site positions per unit cell, at relatively low occupancies on each site. Ten sites were used ($s = 1$–10), at ideal coordinates [0,0,$(s - 1)/10$].

Some Cd data were incorporated into the $\{x, y, z, s\}$ arrays. It was initially assumed that

(i) the X deficiency per unit cell relative to ideal fluorapatite was charge-balanced by removal of Cd: $2X^- + Cd^{2+} = 2\square + \square$ ($\square$ = vacancy);

(ii) the vacancies were all on Cd2 sites, near the X rods;

(iii) there was a maximum of one vacancy per Cd2 triangle.

Points (ii) and (iii) are crystal chemically reasonable assumptions since they minimize local charge imbalance. Since the X deficiency is $2 - q$ per unit cell and there were two Cd2 triangles per cell, $(1 - q/2) = 11\%$ of the triangles contained one vacancy for the Cd–P–Br compound and 18.5% did so for the Cd–V–I compound. No further ordering of the Cd2 vacancies was assumed initially. Note that the average structure data (3) suggest a higher vacancy concentration on Cd2 for the Cd–V–I compound but no preference between Cd1 and Cd2 for Cd–P–Br apatite. Normal values for anisotropic thermal parameters for Cd suggested that relaxation of Cd away from the average positions was not an important structural feature. Small displacements of Cd2 in the model were found to produce additional structure not seen in the experimental patterns. We deduce that such displacements are either negligibly small or not well correlated.

This representation of the structure was used as input to the program DIFFUSE (16) which was run on the Fujitsu vpp300 supercomputer at the ANU Supercomputer Facility. DIFFUSE was used to calculate diffraction patterns for reciprocal lattice sections *hhl* parallel to **c*** and *hkq* normal to **c***, with Bragg peaks subtracted. Small spots of diffuse scattering surrounding the Bragg peak positions were nevertheless observed due to the partial occupancy of the Cd2 sites.

CHARACTERIZATION OF STRUCTURE

The following parameters were calculated in order to characterize the structure of the simulation.

(i) X content. This was the mean number of X per apatite formula unit in the $\{x, y, z, s\}$ array. The value was always found to be $q/2$ within experimental error.

(ii) X substructure order parameters.

(iii) X..Cd coupling parameter.

Short-range order parameters of types (ii) and (iii) are described in more detail below.

X Substructure Order Parameters

These were calculated from the δw displacements of the $\{x,y,w\}$ array.

σ_w = Standard deviation of spacing along the **w** axis: $\langle(\delta w_{xyw+1} - \delta w_{xyw})^2\rangle$.

c_1 = Mean cosine of phase angle between rods neighboring in $\langle 100\rangle$ directions. $\langle\cos 2\pi(t' - t)\rangle$ where absolute height $t = w + \delta w$ for a central atom and t is the closest t value in one of the six neighbouring rods. Unlike parameters such as $\langle\delta t\delta t'\rangle$, this is completely independent of the choice of t origin or total variance of δw.

c_2 = A similar parameter for second-nearest neighbors along $\langle 210\rangle$ directions.

The two parameters c_1 and c_2 take the values $+1$ when all rods are perfectly in phase and 0 when rods are randomly offset relative to their neighbors. Physically attainable values of c_1 and c_2 were found to define an approximately triangular region of a two-dimensional order parameter space. Sharp corners of the triangle corresponded to primitive hexagonal ($c_1 = +1$, $c_2 = +1$) and rhombohedral ($c_1 = -\frac{1}{2}$, $c_2 = +1$) arrangements of X rods. These structures are conveniently identified as "1H" and "3R," respectively, using the polytype notation of Ramsdell (17). The corresponding modulation wavevectors indexed on the fluorapatite cell are (0 0 q) and ($\frac{1}{3}$ $\frac{1}{3}$ q), respectively. The low-c_2, high-c_1 boundary of the order parameter space was found to be delimited by modulated structures with wavevector (r 0 q), $0 < r < \frac{1}{2}$. These have $c_1 = \frac{1}{3}(1 + 2\cos 2\pi r)$, $c_2 = \frac{1}{3}(2\cos 2\pi r + \cos 4\pi r)$. These superstructures are in general C-centered monoclinic in maximum symmetry (I orthorhombic for $r = \frac{1}{2}$). Figure 4 shows examples, along with the locations of the 1H and 3R structures in c_1–c_2 space. Modulated structures with wave vectors ($\frac{1}{3} + \lambda$ $\frac{1}{3} - 2\lambda$ q), intermediate between 3R ($\frac{1}{3}$ $\frac{1}{3}$ q) and 2O ($\frac{1}{2}$ 0 q) cases, lie along an almost straight line connecting these extremes. Structures with wavevector (r r q), $0 < r < \frac{1}{3}$, intermediate between 1H and 3R, were found to lie along a curve that closely parallelled $1H \rightarrow 2O \rightarrow 3R$ but lay inside it.

X..Cd Coupling Parameter

It was found that the split-site occupancies of (3) were modeled well if a cosine potential $-E_{Cd,0}\cos 4\pi z$ was assumed, with X anion z coordinates distributed proportional to $\exp(-E_{Cd,0})$. The parameter $E_{Cd,0}$ was defined as the amplitude of the cosine potential producing a given degree of fractionation between split sites *in the absence of other perturbing potentials*. $E_{Cd,0}$ provides a convenient single-parameter measure of long-range order of z coordinates for X anions. The fitted value was $-0.51\ kT$ for the Cd–V–I compound and $-1.06\ kT$ for the Cd-P-Br phase. The occupancies of Table 2 show that the real structure has slightly higher occupancy in sites 2–3 and lower occupancy in the other sites than can be accounted for with a pure cosine potential. Nevertheless, the fit is close without the

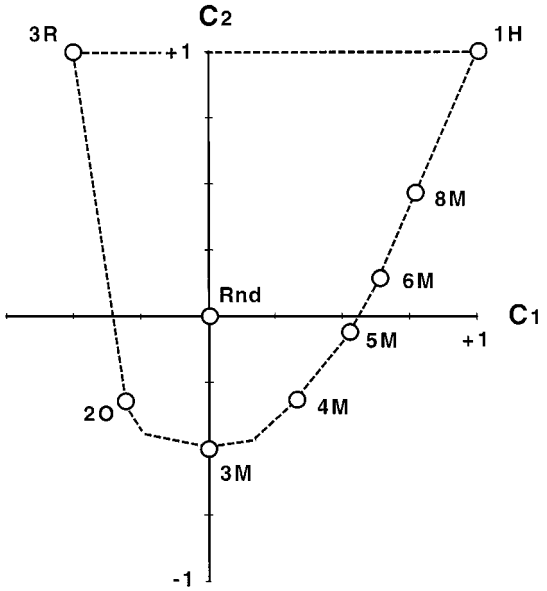

FIG. 4. c_1–c_2 order parameter space, showing locations of different ordered X substructures.

TABLE 2
$E_{Cd,0}$ Fits to Split-Site X Occupancy Data

	Cd–V–I		Cd–P–Br		Cd–P–Br	
	Exp[a]	Fit	Exp[a]	Fit	Exp[c]	Fit
$E_{Cd,0}$		−0.514		−1.056		−0.735
Site 1, $z = 0.25$	0.090	0.128	0.122	0.184	0.127	0.145
Site 2, $z = 0.20$	0.236	0.232	0.353	0.300	0.253	0.253
Site 3, $z = 0.15$	0.160	0.179	0.213	0.177	0.249	0.176
Site 4, $z = 0.10$	0.152	0.130	0.086	0.092	0.127	0.113
Site 5, $z = 0.05$	0.098	0.101	0.041	0.054	0.082	0.078
Site 6, $z = 0.00$	-0.003[b]	0.046	0.014	0.022	0.000	0.034
Rms error		0.029		0.037		0.016

[a] Sudarsanan *et al.* (3).
[b] Set to zero for fitting.
[c] Calculated from Alberius-Henning *et al.* (1, 6).

need to introduce additional terms into the potential function. For comparison of the long-range order in simulations, the z coordinates of X in the simulation were rebinned into six symmetrically distinct sites per cell corresponding to those of of (3) and entered into a fitting program to calculate the corresponding value of $E_{\mathrm{Cd},0}$. It was found that the actual value of E_{Cd} required to produce the occupancies matching a given $E_{\mathrm{Cd},0}$ depended strongly on the values of the other interaction parameters. For fixed values of the other parameters, E_{Cd} was nearly a linear function of $E_{\mathrm{Cd},0}$, but the constant of proportionality varied nonlinearly with the other interactions. A complication in fitting the experimental data was that the occupancy data of (3) were collected at an unspecified temperature, presumed to be about 298 K, and not at 150 K as were the data of this study. If all interaction parameters E_x, E_y, E_z, and E_{Cd} are assumed independent of temperature when measured in joules, and hence inversely proportional to temperature when measured in kT, then all ratios of parameters such as E_x/E_z, E_{Cd}/E_z are also invariant. However, it cannot be predicted *a priori* how the order parameter $E_{\mathrm{Cd},0}$ varies if all interaction parameters are scaled uniformly. Additional simulations were run in order to investigate this matter. Note that the split-site distribution corresponding to the Cd–P–Br apatite refinement of (1, 6) was best fitted to a value of $E_{\mathrm{Cd},0} = -0.74\,kT$ (Table 2), appreciably smaller than the room-temperature value, in contrast to expectations. Simulations run with small E_{Cd} gave incorrect relative intensities for the different layers of diffuse scattering, implying that the small $E_{\mathrm{Cd},0}$ is an artifact of the truncated sawtooth modulation used in that structure refinement (see below).

RESULTS

Incommensurate Layers Due to E_z

A set of simulations was run with $E_x = E_y = E_{\mathrm{Cd}} = 0$, $E_z \neq 0$ to verify that E_z interactions produce incommensurate layers with no further structure. Three of these are shown in Fig. 5, where it can be seen that increasing E_z indeed produces progressively sharper layers, as the variance σ_w decreases. Although small E_z and large σ_w should prevent the attainment of the maximum possible X content for a given q value, this effect was found to be insignificant for $E_z = 0.1\ kT$. All compositions had $(1 - \eta) = q/2 = 0.890 \pm 0.005$. The low occupancies of (3), which are about 90% of the theoretical maximum values, do not appear to be consequences of this effect, but may be artifacts arising from the deconvolution of the split atoms. Data for the simulations are given in Table 3 under run numbers 1–3.

Ordering Due to E_x and E_y

Figure 6 shows the intensity distribution within a diffuse layer as a function of E_x, with $E_y = E_{\mathrm{Cd}} = 0$, $E_z = +1$.

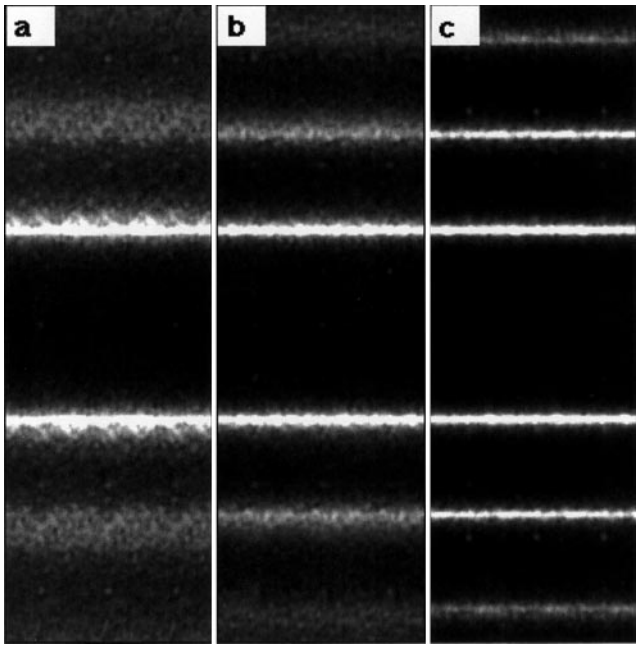

FIG. 5. Calculated *hhl* diffraction patterns for $q = 1.78$, $E_x = E_y = E_{\mathrm{Cd}} = 0$. (a) Run 1, $E_z = +0.2$. (b) Run 2, $E_z = +1.0$. (c) Run 3,R$E_z = +5.0$.

Figure 6a with $E_x = 0$ shows Laue monotonic scattering plus faint modulation that is largely calculation artifacts. In Fig. 6b, $E_x < 0$ produces diffuse spots at integral h and k values (i.e., the $1H$ structure). $E_x > 0$ produces a

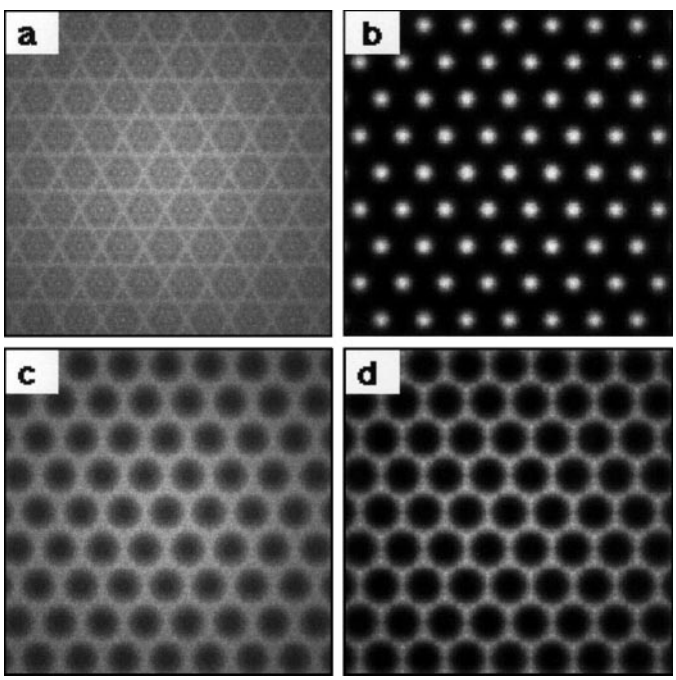

FIG. 6. Calculated *hkq* patterns with $q = 1.78$, $E_y = E_{\mathrm{Cd}} = 0$, $E_z = +1$. Symmetry is imposed by averaging. (a) Run 2, $E_x = 0$. (b) Run 4, $E_x = -1.0$. (c) Run 5, $E_x = +0.2$. (d) Run 6, $E_x = +1.0$.

honeycomb pattern with no discrete spots (Figs. 6c, 6d). In Fig. 7, the pattern of Fig. 6d undergoes further condensation due to nonzero E_y interactions. $E_x < 0$, $E_y > 0$ causes condensation near ($\frac{1}{2}$ 0 q) and related points to give an incipient $2O$ superstructure (Fig. 7b). $E_y < 0$ causes condensation near ($\frac{1}{3}$ $\frac{1}{3}$ 0) (Figs. 7c, 7d), ultimately forming the $3R$ superstructure. Two other types of layers are shown in Figs. 7e, 7f, corresponding to the cases $E_x = 0$ and $E_x > 0$ for $E_y > 0$. Although not found for the compounds of this study, they might occur in related systems. The modulation vectors are approximately ($\frac{1}{3}$ 0 q) and ($\frac{1}{4}$ 0 q), respectively. Numerical data for these simulations are numbers 2, 4–11 in Table 3.

Ordering Due to E_{Cd}

Figure 8 shows *hhl* diffraction patterns calculated with $E_{Cd} = 0$, -1.0, and -5.0. Note that the first obvious effect of E_{Cd} is to transfer intensity from the layer at $l = 2q$ to a new layer at $l = q + 2$ (Fig. 8b). For larger values (Fig. 8c) additional layers at $l = 2, 4 - q, 2q - 2$, and so on start to appear.

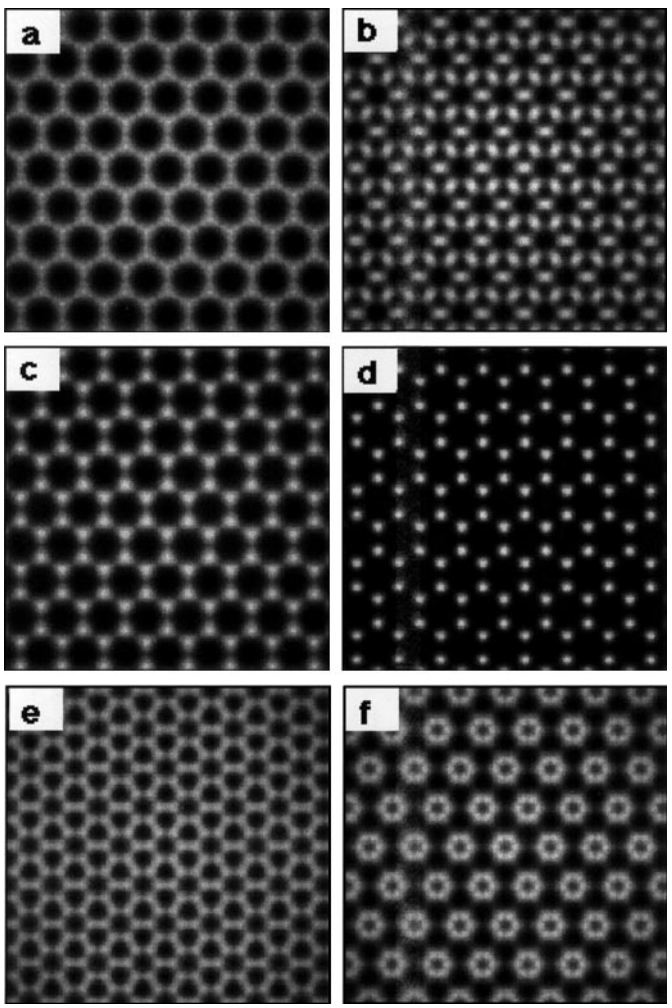

FIG. 7. Calculated *hkq* patterns with $q = 1.78$, $E_x = +1$, $E_{Cd} = 0$, $E_z = +1$. Symmetry is imposed by averaging. (a) Run 6, $E_y = 0$. (b) Run 7, $E_y = +1.0$. (c) Run 8, $E_y = -0.2$. (d) Run 9, $E_y = -1.0$. (e) Run 10, $E_y = +1.0$, $E_x = 0$. (f) Run 11, $E_y = +1.0$, $E_x = -1$.

TABLE 3
Input and Output Parameters for Simulations Discussed in the Text

Run no.	q	E_x	E_y	E_z	E_{Cd}	σ_w	c_1	c_2	$E_{Cd,0}$
1	1.78	0	0	+0.2	0	0.152	−0.003	+0.007	0
2	1.78	0	0	+1	0	0.098	-0.006	+0.010	0
3	1.78	0	0	+5	0	0.051	−0.010	+0.016	0
4	1.78	−1	0	+1	0	0.092	+0.468	+0.245	0
5	1.78	+0.2	0	+1	0	0.098	−0.084	+0.017	0
6	1.78	+1	0	+1	0	0.093	−0.220	+0.106	0
7	1.78	+1	+1	+1	0	0.092	−0.136	−0.183	0
8	1.78	+1	−0.2	+1	0	0.092	−0.242	+0.198	0
9	1.78	+1	−1	+1	0	0.090	−0.305	+0.489	0
10	1.78	0	+1	+1	0	0.093	−0.008	−0.216	0
11	1.78	−1	+1	+1	0	0.092	+0.203	−0.145	0
12	1.78	+1	0	+1	−1	0.101	−0.176	+0.122	−0.38
13	1.78	+1	0	+1	−5	0.211	+0.547	+0.587	−3.43
14	1.78	0	0	+1	−1	0.125	+0.122	+0.123	−0.83
15	1.78	0	0	+1	-2	0.172	+0.374	+0.381	−1.85
16	1.78	0	0	+1	−3	0.207	+0.561	+0.567	−3.25
17	1.78	0	0	+2	−1	0.093	+0.052	+0.067	−0.53
18	1.78	0	0	+2	−2	0.132	+0.215	+0.229	−1.16
19	1.78	0	0	+2	−3	0.170	+0.406	+0.416	−1.92
20	1.78	+1	0	+1	−2	0.124	−0.036	+0.186	−0.84
21	1.78	+1	0	+1	−3	0.156	+0.174	+0.310	−1.44
22	1.63	0	0	+1	−1	0.108	+0.016	+0.017	−0.35
23	1.63	0	0	+1	−2	0.134	+0.076	+0.076	−0.72
24	1.63	0	0	+1	−3	0.163	+0.157	+0.162	−1.08
25	1.63	0	0	+2	−1	0.082	+0.008	+0.009	−0.21
26	1.63	0	0	+2	−2	0.097	+0.030	+0.034	−0.43
27	1.63	0	0	+2	−3	0.117	+0.071	+0.067	−0.65
28	1.63	+1	0	+1	−1	0.099	−0.201	+0.109	−0.24
29	1.63	+1	0	+1	−2	0.115	−0.152	+0.114	−0.50
30	1.63	+1	0	+1	−3	0.137	−0.073	+0.135	−0.76
31	1.63	+0.25	0	+2	−2.55	0.105	−0.032	+0.058	−0.52
32	1.63	+0.5	0	+4	−5.1	0.103	−0.035	+0.083	−0.59
33	1.78	+0.5	−0.25	+1	−1.6	0.134	+0.074	+0.273	−1.06
34	1.78	+1	−0.5	+2	−3.2	0.143	+0.137	+0.381	−1.34
35	1.63	+0.5	0	+4	0	0.056	−0.152	+0.038	0
36	1.78	+1	−0.5	+2	0	0.072	−0.274	+0.316	0
37	1.63	0	0	+4	−5.1	0.109	+0.067	+0.089	−0.64
38	1.78	0	0	+2	−3.2	0.176	+0.436	+0.456	−2.07

If $E_{Cd} = 0$, there is a uniform distribution of X anion z coordinates. The ordering quasi-energy $E_{Cd,0}$ is therefore zero as well. Negative E_{Cd} allows attainment of negative $E_{Cd,0}$, but $|E_{Cd,0}| < |E_{Cd}|$, implying that ordering is impeded by the $X..X$ interactions. $E_{Cd,0}$ is plotted as a function of E_{Cd} for different E_x, E_z, and q values in Fig. 9. Run numbers in Table 3 are 10 and 13–19 ($q = 1.78$) and 20–28 ($q = 1.63$). Note that for a given state of order $E_{Cd,0}$, the E_{Cd} needs to be about twice as large for $q = 1.63$ as for $q = 1.78$. Clearly, the ability of $X..X$ interactions to disrupt commensurate superstructure formation increases with the deviation away from commensurability $|2 - q|$. Conversely, the c_1 and c_2 data for these runs become more positive as $|E_{Cd}|$ increases, showing

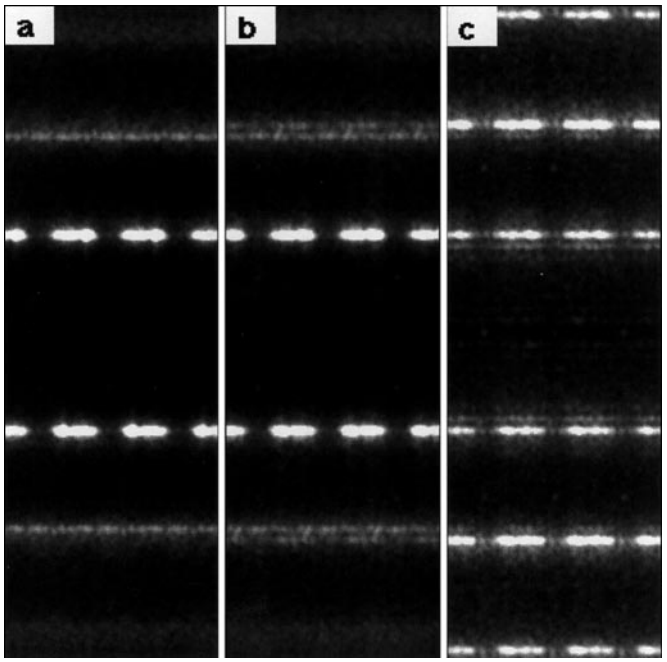

FIG. 8. Calculated *hhl* diffraction patterns for $q = 1.78$, $E_x = +1$, $E_y = 0$, $E_z = +1$. (a) Run 6, $E_{Cd} = 0$. (b) Run 12, $E_{Cd} = +1$. (c) Run 13, $E_{Cd} = +5$.

that the tendency to lock into the Cd substructure forces neighboring X rods into phase with each other.

Figure 10 shows plots of E_{Cd} against E_z at constant $E_{Cd,0}$. These are examples of runs that were used to investigate the behavior of $E_{Cd,0}$ as the other parameters are uniformly scaled, simulating the effect of temperature change. It can be seen that for $q = 1.78$, moving radially away from the origin (decreasing temperature) increases $E_{Cd,0}$. The change is greatest if E_{Cd} is large relative to other parameters. For $q = 1.63$, the contours are steeper, and the temperature dependence of $E_{Cd,0}$ is smaller.

Additional Ordering of Cd Vacancies

A simulation in which an additional energy term placed $Cd_2\square$ triangles preferentially farther away from X but Cd_3 triangles closer to X showed no discernible change in the extended diffuse features. However, the small diffuse spots surrounding Bragg positions became fainter. It appears that the experimental patterns do not provide useful information on such ordering.

Possible Size Effect Due to Cd2 Triangles

An extension to the DIFFUSE input subroutine was tried, in which Cd2 triangles expanded or contracted by a small amount (1%) depending on the relative height of the nearest X anion. Even this small change caused considerable additional contrast within the *hkq* diffuse layer, strongly enhancing the intensity of a hexagonal central region. The absence of such structure in the experimental data suggests that there is no strong coupling of Cd displacements in the xy plane to z displacements of X.

Overall

Figure 11 shows a c_1–c_2 plot for runs 2, 4–13. The effect of varying E_x from negative to positive is to move in an arc away from $1H$ and toward the $2O$–$3R$ line $4 \rightarrow 2 \rightarrow 5 \rightarrow 6$. Changing E_y from negative to positive causes a move away from the $3R$ corner $9 \rightarrow 8 \rightarrow 6 \rightarrow 7$. Change in the r component of $[r\ 0\ q]$ modulation vectors with E_x for $E_y > 0$ is shown by $6 \rightarrow 10 \rightarrow 11$. Increasing E_{Cd} from zero causes a move toward $1H$, $6 \rightarrow 12 \rightarrow 13$.

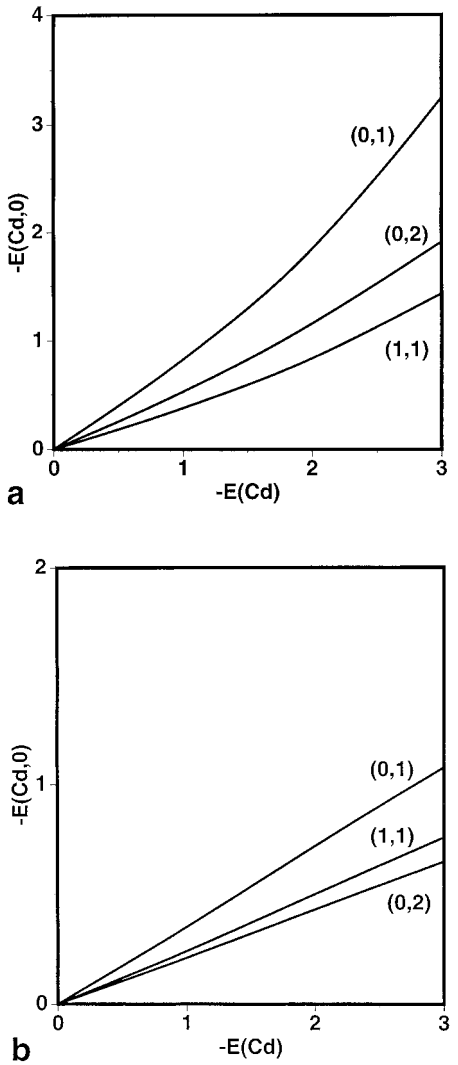

FIG. 9. Plots of $E_{Cd,0}$ against E_{Cd} for (a) $q = 1.78$ and (b) $q = 1.63$. Numbers in parentheses are (E_x, E_z). $E_y = 0$.

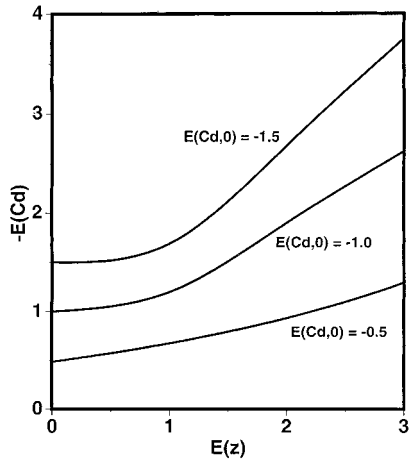

FIG. 10. Contours of constant $E_{Cd,0}$ for $q = 1.78$, $E_x = E_y = 0$.

Quantitative Fitting of Apatite Data

Since $E_{Cd,0}$ could only be fitted retrospectively to the split-site occupancy from a run, reconnaissance simulations were run in order to map its variation as a function of E_x, E_y, and E_z. It was then possible to choose a value of E_{Cd} for any combination of q, E_x, E_y, and E_z that gave an appropriate value of $E_{Cd,0}$. Note that both $2q$ and $q + 2$ diffuse layers are apparent in the original experimental *hhl* diffraction patterns. The $2q$ layer is stronger for Cd–V–I apatite by a factor of about 2, whereas the converse is true for Cd–P–Br apatite. The relative intensities of the two layers were found empirically to depend most strongly on the E_{Cd}/E_z ratio, which in turn correlated with E_x/E_z for a constant value of $E_{Cd,0}$. Matching the degree of condensation within the layers provided a further constraint on the magnitude of E_x (honeycomb sharpness) and E_y (spot condensation). Surprisingly, E_y/E_z was found to be a better predictor of spot sharpness than E_y/E_x.

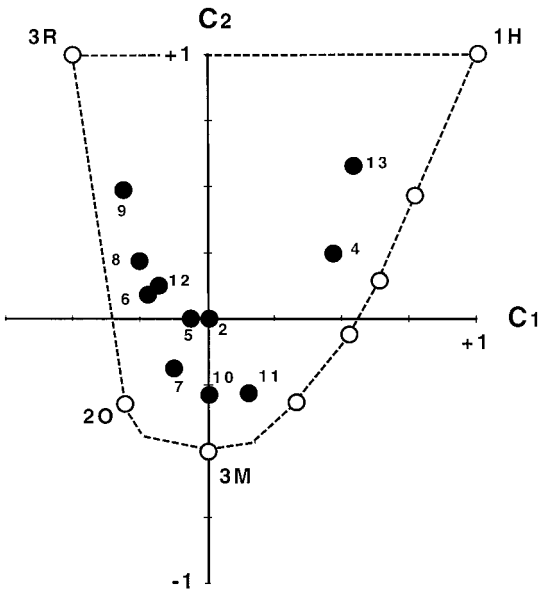

FIG. 11. c_1–c_2 plot for runs 2, 4–13.

The temperature difference between the experimental data of (1, 6) and this study and that of (3) was addressed as follows. It was initially assumed that the absolute magnitudes of the interaction energies remained constant. Values of E_x, E_y, and E_z were found that fit the low-temperature diffuse pattern well. These were then halved, simulating doubling of the absolute temperature, and iteration and interpolation were used to obtain E_{Cd} values that gave $E_{Cd,0}$ appropriate for the occupancies of (3). Those E_{Cd} values were then doubled to give values appropriate for the low-temperature E_x–E_z. The corresponding $E_{Cd,0}$ values for 150 K were found to be only slightly larger than the high-temperature values. The change with temperature in long-range order of z_X distribution is evidently small unless the interaction parameters are strongly temperature-dependent.

For Cd–V–I apatite, E_y was maintained equal to zero. Sharpness of the honeycomb texture was found to be best matched for $E_x = +0.5$. In order to check the relative intensities of $2q$ and $q + 2$ layers, a computer program was written to average intensity along the layers in the calculated images and fit Gaussian profiles to them. $I(2q)/I(q + 2)$ increased strongly with E_z up to $E_z = +4$ and declined again to 1.53 at $E_z = +5$, so $E_z = +4.0$ was taken to be the optimal 150 K value. Fitting $E_{Cd,0}$ for room-temperature simulations with $E_x = +0.25$, $E_z = +2.0$ gave $E_{Cd} = -2.55$ (298 K), -5.1 (150 K).

For the Cd–P–Br phase, $E_y = -\frac{1}{4}E_z$ to $-\frac{1}{2}E_z$ was found to give the correct degree of spot condensation. $E_x < \frac{2}{3}E_z$ was needed to prevent excessively strong $q + 2$ layers and supernumerary layers from appearing. This corresponded to an approximate upper limit on E_{Cd}/E_z of 1.6, almost independent of E_y. Large $|E_y|/E_x$ (> 0.5) and E_z (> 4) were also found to enhance spurious satellite peaks. For small magnitudes of energies, the window of appropriate E_x:E_y:E_y ratios was very narrow. The best fits to the experimental pattern were obtained with $E_x = +1$, $E_y = -0.5$, and $E_z = +2$. Room-temperature runs with halved parameter values gave $E_{Cd} = -1.6$, E_{Cd} (150 K) $= -3.2$. Simulations with the smaller $E_{Cd,0}$ calculated from the refinement (1, 6) had $2q$ and $q + 2$ layers of nearly equal intensity, whereas the experimental data has the $q + 2$ intensity much larger than the $2q$. There is evidently more concentration of Br toward $z = \pm 0.25$ than is predicted by the truncated sawtooth modulation model.

Data for the best fitting simulations (at 150 K and 298 K) are shown in Table 3 as runs 31–34. Calculated diffraction patterns are shown in Fig. 12 for 150 K. The 298 K versions are noticeably more diffuse but otherwise similar.

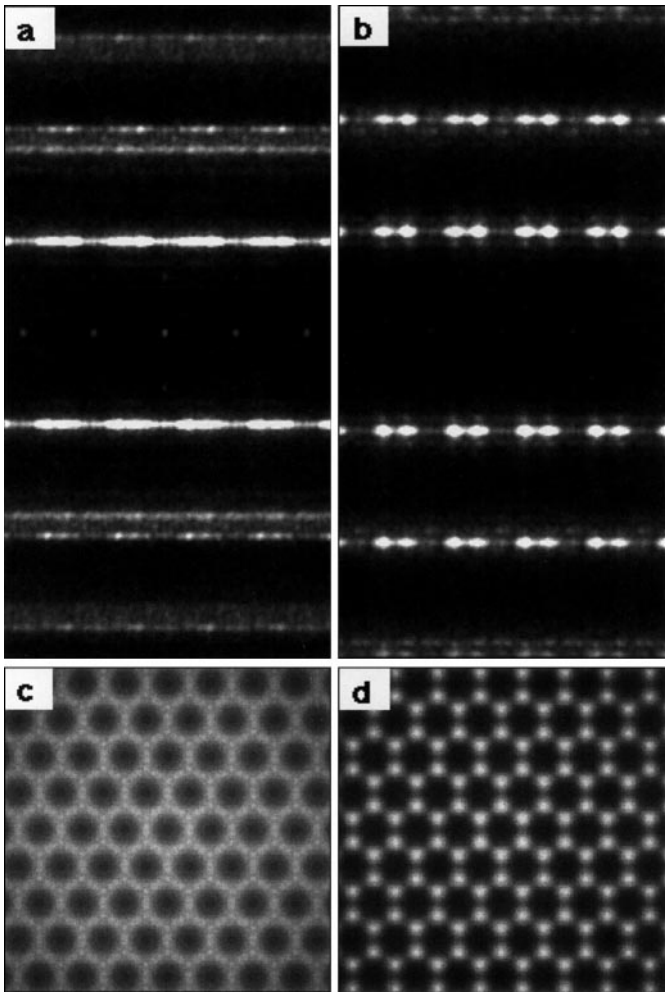

FIG. 12. Best simulations for 150 K experimental patterns. *hhl* patterns: (a) run 31 and (b) run 32. *hkq* patterns: (c) run 31 and (d) run 32.13.

The disordering effect of E_{Cd} on c_1 is demonstrated by runs 35 and 36 (Table 3), analogues of runs 32 and 34 but with E_{Cd} set to zero. These simulations are shown, along with the 150 K and 298 K fits, in the c_1–c_2 plot of Fig. 13. It is evident that in the absence of a Cd..X interaction, the X substructures of both compounds would be ordered to about half the maximum possible extent, Cd–P–Br apatite in the direction of 3R and Cd–V–I intermediate between 3R and 2O. Runs 37 and 38 (Table 3) show the effect of E_x and E_y on $E_{Cd,0}$. They make explicit the increases in c_1 and c_2 due to E_{Cd}, and demonstrate the considerable reduction in $E_{Cd,0}$ brought about by small E_x and E_y interactions.

Energetics

At the temperature of data collection (150 K), the unit of energy $kT = 1.25$ kJ/mol. Values for the interaction energies of the best fitting simulations are given with estimated uncertainties in Table 4. Several features of interest are to be noted.

(i) The X..X interaction E_z, at 2–5 kJ/mol, is quite typical in magnitude for a strong van der Waals interaction or a "nonbonded" interaction between two atoms sharing a common ligand. E_z is bigger for the iodide, as would be expected from both the lower q (halide anions more compressed by Cd–T–O host) and the higher atomic numbers (van der Waals forces stronger).

(ii) The X..Cd interaction E_{Cd} is similar in magnitude to but somewhat larger than E_z for both compounds. The factor of 2 difference in $E_{Cd,0}$ and the factor of ca. 4 difference in intensity ratio of the $2q$ and $q + 2$ diffuse layers arise mainly because $|2 - q|$, the deviation from commensurability, is much larger for the iodide than for the bromide. Therefore, the incipient superstructure determined by X..X interactions is perturbed less by E_{Cd} in Cd–V–I apatite, and it is more difficult for E_{Cd} to perturb the iodides toward the Cd2 triangles.

The amplitude $2|E_{Cd}|$ is effectively the energy difference per halide between an apatite with octahedrally coordinated X at $z_{ap} = 0$ and a triangular-coordinated X at $z_{ap} = 0.25$. The effective standard dissociation enthalpy for a unit-order Cd–X bond in a solid can be estimated as that for the reaction $\frac{1}{2}CdX_2(s) \rightarrow \frac{1}{2}Cd(g) + X(g)$, which is 270 kJ/mol ($X$ = Br) or 208 kJ/mol (X = I) using literature values for the thermodynamic data (18, 19). Hence, E_{Cd} is about 1/50 of a unit-order Cd–X bond enthalpy, which is eminently reasonable. Note that the amplitude is nearly twice as great for the iodide, which seems counterintuitive since it should be sterically more unfavorable for I to approach coplanarity with the Cd2 triangle than for Br to do so. A possible

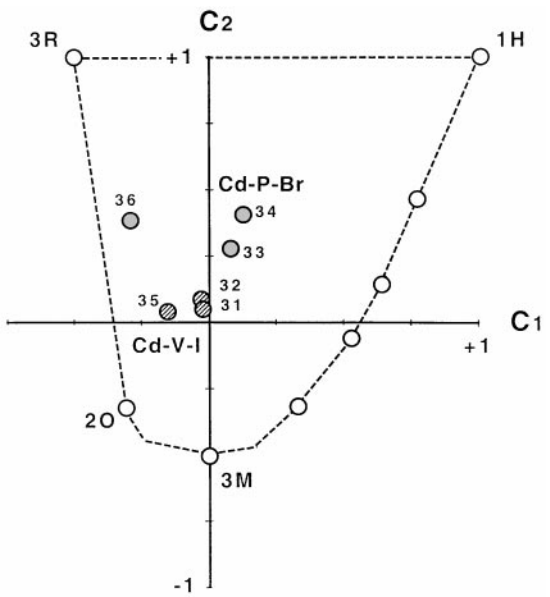

FIG. 13. c_1–c_2 plot for runs 31–36.

TABLE 4
Numerical Values for Interaction Energies (kJ/mol)

	Cd–V–I	Cd–P–Br
E_x	+ 0.6(2)	+ 1.3(2)
E_y	0.0(2)	− 0.6(2)
E_z	+ 5.0(13)	+ 2.5(6)
E_{Cd}	− 6.4	− 4

explanation is that the sinusoidal potential in Cd–P–Br apatite is damped due to the very short c axis (10% shorter than in the Cd–V–I phase).

(iii) $X..X$ interactions along $\langle 100 \rangle$ vectors may be as big as 1500 J/mol, and along $\langle 210 \rangle$ as big as 800 J/mol. These values are extremely large given the large $X..X$ distances are approximately 10 Å and 17 Å, respectively. Topologically, the $\langle 100 \rangle$ halides are actually sixth-nearest neighbors, connected by a chain of Cd, O, and T atoms. The importance of relaxations of these species (14, 15) as mediators is reinforced, propagating local bond-valence distortions, without contributing significantly to the X-ray diffuse scattering pattern.

DISCUSSION

The Cd apatites of this study are chimney–ladder structures with one-dimensional incommensuration of "chimney" Cd-T-O framework and "ladder" columns of X atoms, but with the additional complication that the z offsets of neighboring ladders are correlated so as to form incipient nonprimitive superstructures. The $< 100 >$ repulsions that drive this ordering are surprisingly strong given the 10 Å separation between rods, being of the same order of magnitude as the short-range $X..X$ and X..Cd interactions along **c**. If the $\langle 100 \rangle$ $X..X$ interactions were attractive, tending to form a primitive array of X anions, then $X..X$ and X..Cd interactions would mutually reinforce to form a conventional Nowotny-type chimney–ladder, possibly with Vernier commensurability. However, in the apatites of this study, $\langle 100 \rangle$ repulsions cause a chimney–ladder structure with mutually frustrating chimney–chimney and chimney–ladder interactions. The frustration is reflected in the diffraction pattern, which shows diffuse superstructure features only, including two second-order layers at $l = 2q$ and $q + 2$.

It is likely that similar short-range ordering is present in chemically related apatites. Sudarsanan *et al.* (3) report three-dimensional structural data for the Cd–As–Br, Cd–V–Br, and even Cd–P–Cl that show low total halide occupancies and delocalization of halides in the three-dimensional long-range average structure. These and other analogues of the apatites of this study evidently need further X-ray study with an area detector.

The values for E_{Cd} and E_z obtained in this study allow estimation of the effective activation energy E_a for diffusion of X anions along the $\langle 001 \rangle$ rods. Since the interaction parameters correspond approximately to two mutually incommensurate sinusoidal potentials of amplitude $\frac{1}{2}E_z$ and E_{Cd}, $E_a \approx 2 \times \sqrt{(\frac{1}{4}E_z^2 + E_{Cd}^2)} = 4$–$7$ kJ/mol. This value, effectively the energy difference between an anion in a triangular site and in an octahedral site, is an order of magnitude lower than the activation energy of 0.77 eV = 74 kJ/mol calculated for fluoride vacancy diffusion along **c** in fluorapatite (20), which is reasonable given the smaller bonded radius of F^- and its marked preference for the triangular coordinated site. Our estimated E_a is nearly 2 orders of magnitude lower than published activation energies (ca. 200 kJ/mol) for the more complex processes of diffusional exchange of $F^-/OH^-/Cl^-$ and O^{2-} in apatites (21, 22). It is possible that the apatites of this study are ionic conductors in the **c** direction. E_a values for other ionically conducting systems are 41–50 kJ/mol for Cu–Fe sulfides (23), 15 kJ/mol in Na β-alumina, and 5 kJ/mol in α-AgI (24). However, the charge carrier in most known ionic conductors is a small cation (Li^+, Na^+, Cu^+, Ag^+) or anion (O^{2-}, F^-) whereas large anions (Br^-, I^-) would be mobile in the apatites. The apatites are also interesting in that the anion mobility is one-dimensional along **c** (in β-alumina solid electrolyes, cation mobility is in the xy plane). Clearly, the dielectric and conductivity properties of these compounds would also repay further investigation.

ACKNOWLEDGMENTS

A.G.C. thanks Richard Welberry for the award of a Visiting Fellowship at the Research School of Chemistry, Australian National University. We thank the ANU Supercomputer Facility for the grant of time on the Fujitsu vpp300. This manuscript was much improved after thorough reading and constructive comments by Lasse Norén and two anonymous referees.

REFERENCES

1. P. Alberius-Henning, Modulating the anion ordering in apatites, Ph.D. thesis. University of Stockholm, 1999.
2. S. Náray-Szabó, *Z. Kristallogr.* **75,** 387 (1930).
3. K. Sudarsanan, R. A. Young, and A. J. C. Wilson, *Acta Crystallogr. B* **33,** 3136 (1977).
4. R. D. Shannon, *Acta Crystallogr. A* **32,** 751 (1976).
5. A. J. C. Wilson, K. Sudarasan, and R. A. Young, *Acta Crystallogr. B* **33,** 3142 (1977).
6. P. Alberius-Henning, M. Moustiakimov, and S. A. Lidin, *J. Solid State Chem.* **150,** 154 (1999).
7. W. B. Pearson, *Acta Crystallogr. B* **26,** 1044 (1970).
8. H. Völlenkle, A. Preisinger, H. Nowotny, and A. Wittmann, *Z. Kristallogr.* **124,** 9 (1967).
9. H. Nowotny, *in* "The Chemistry of Extended Defects in Non-metallic solids" (L. Eyring and M. O'Keeffe, Eds.). North-Holland, Amsterdam. 1970.
10. R. J. Nelmes, D. R. Allen, M. I. McMahon, and S. A. Belmonte, *Phys. Rev. Lett.* **83,** 4081 (1999).

11. H. Böhm and H.-G. von Schnering, *Z. Kristallogr.* **171,** 41 (1985).
12. I. D. Brown, B. D. Cutforth, C. G. Davies, R. J. Gillespie, P. R. Ireland, and J. E. Vekris, *Can. J. Chem.* **52,** 791 (1975).
13. T. R. Welberry and S. C. Mayo, *J. Appl. Crystallogr.* **29,** 353 (1996).
14. K. Sudarsanan and R. A. Young, *Acta Crystallogr. B* **34,** 1401 (1978).
15. V. P. Orlovskii and S. P. Ionov, *Russ. J. Inorg. Chem.* **40,** 1884 (1995).
16. B. D. Butler and T. R. Welberry, *J. Appl. Crystallogr.* **25,** 391 (1992).
17. L. S. Ramsdell, *Am. Mineral.* **32,** 64 (1947).
18. D. D. Wagman, W. H. Evans, V. B. Parker, R. H. Schum, I. Halow, S. M. Bailey, K. L. Chaney, and R. L. Nuttall, *J. Phys. Chem. Ref. Data* **11,** Suppl. 2 (1982).
19. D. R. Lide, Ed., "CRC Handbook of Chemistry and Physics," 79th ed. CRC Press, Boca Raton, 1998.
20. D. O. Welch and B. S. H. Royce, *Phys. Status Solidi B* **57,** 193 (1973).
21. J. Brenan, *Chem. Geol.* **110,** 195 (1993).
22. J. R. Farver and B. J. Giletti, *Geochim. Cosmochim. Acta* **53,** 1621 (1989).
23. R. Berger and R.V. Buchur, *Solid State Ionics* **89,** 269 (1996).
24. A. R. West, "Basic Solid State Chemistry," Wiley, Chichester, 1984.